JACS
JOURNAL OF THE AMERICAN CHEMICAL SOCIETY

Article

pubs.acs.org/JACS

Charge Dissociation at Interfaces between Discotic Liquid Crystals: The Surprising Role of Column Mismatch

Julien Idé,[†,‡] Raphaël Méreau,[†] Laurent Ducasse,[†] Frédéric Castet,[†] Harald Bock,[§] Yoann Olivier,[∥] Jérôme Cornil,[∥] David Beljonne,[∥] Gabriele D'Avino,*[,⊥,#] Otello Maria Roscioni,[⊥] Luca Muccioli,[⊥] and Claudio Zannoni[⊥]

[†]Institut des Sciences Moléculaires, UMR CNRS 5255, Université de Bordeaux, Cours de la Libération 351, FR-33405 Talence, France

[‡]Dipartimento di Chimica, Materiali e Ingegneria Chimica "G. Natta", Politecnico di Milano, via Mancinelli 7, IT-20131 Milano, Italy

[§]Centre de Recherche Paul Pascal, UPR CNRS 8641, Université de Bordeaux, Avenue Schweitzer 115, FR-33600 Pessac, France

[∥]Laboratory for Chemistry of Novel Materials, University of Mons, Place du Parc 20, BE-7000 Mons, Belgium

[⊥]Department of Industrial Chemistry "Toso Montanari" and INSTM, University of Bologna, Viale del Risorgimento 4, IT-40136 Bologna, Italy

Supporting Information

ABSTRACT: The semiconducting and self-assembling properties of columnar discotic liquid crystals have stimulated intense research toward their application in organic solar cells, although with a rather disappointing outcome to date in terms of efficiencies. These failures call for a rational strategy to choose those molecular design features (e.g., lattice parameter, length and nature of peripheral chains) that could optimize solar cell performance. With this purpose, in this work we address for the first time the construction of a realistic planar heterojunction between a columnar donor and acceptor as well as a quantitative measurement of charge separation and recombination rates using state of the art computational techniques. In particular, choosing as a case study the interface between a perylene donor and a benzoperylene diimide acceptor, we attempt to answer the largely overlooked question of whether having well-matching donor and acceptor columns at the interface is really beneficial for optimal charge separation. Surprisingly, it turns out that achieving a system with contiguous columns is detrimental to the solar cell efficiency and that engineering the mismatch is the key to optimal performance.

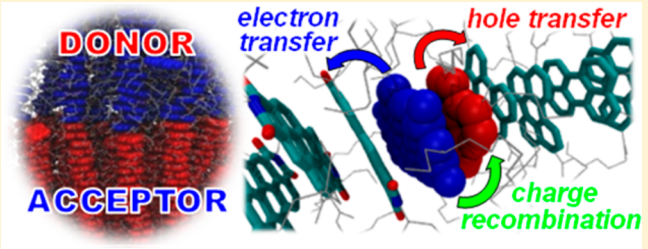

INTRODUCTION

Organic solar cells (OSCs) are devices invariably based on interfacing a conjugated electron donor (an organic p-type semiconductor, D) with an electron acceptor (an n-type semiconductor, A), both of which are able to absorb at least a portion of the solar spectrum. In principle, the fraction of sun-generated excitons able to reach the D−A interface can there dissociate and be transformed into hole−electron pairs, which subsequently should separate and move to the electrodes, generating a current. In practice, the finite lifetime of (singlet) excitons severely limits the average distance they can travel before they decay to the ground state (L_d) with typical values of about 5 nm for polymers,[1] 20 nm for small molecules in thin crystalline films,[2] and 50 nm for columnar liquid crystals.[3−5] This limitation has stimulated the development of bulk-heterojunction cells, where the donor−acceptor contact surface is maximized and the size of the D and A domains, which are often amorphous, is comparable to L_d.[6]

An alternative route to improve the conversion efficiency by increasing both the exciton diffusion length and the charge carrier mobility is to extend the structural order to larger scales inside a planar heterojunction, choosing donor and acceptor materials that can spontaneously self-assemble into liquid-crystalline phases.[7] Discotic columnar liquid crystals (DLCs) are promising materials for OSCs since they present long exciton diffusion lengths (about 50−100 nm[5,8]) and relatively high charge carrier mobilities along the columns (up to 1 $cm^2 V^{-1} s^{-1}$) compared with conventional disordered materials[9−13] and also by virtue of the tunability of their properties through molecular design (e.g., acting on the nature and size of the aromatic cores and side chains[14,15]).

For a given couple of D and A mesogens, the conversion efficiency of OSCs depends primarily on the morphology of the D−A interface, where the exciton dissociation takes place. There are several factors that must be controlled to achieve an ideal D−A planar interface: (i) the columns should be oriented homeotropically, that is, with the column axis perpendicular to the electrode surfaces and to the interface;[16] (ii) dewetting should be avoided, for example with the help of polar side

Received: August 14, 2013
Published: January 24, 2014

   dx.doi.org/10.1021/ja4114769 | J. Am. Chem. Soc. 2014, 136, 2911−2920

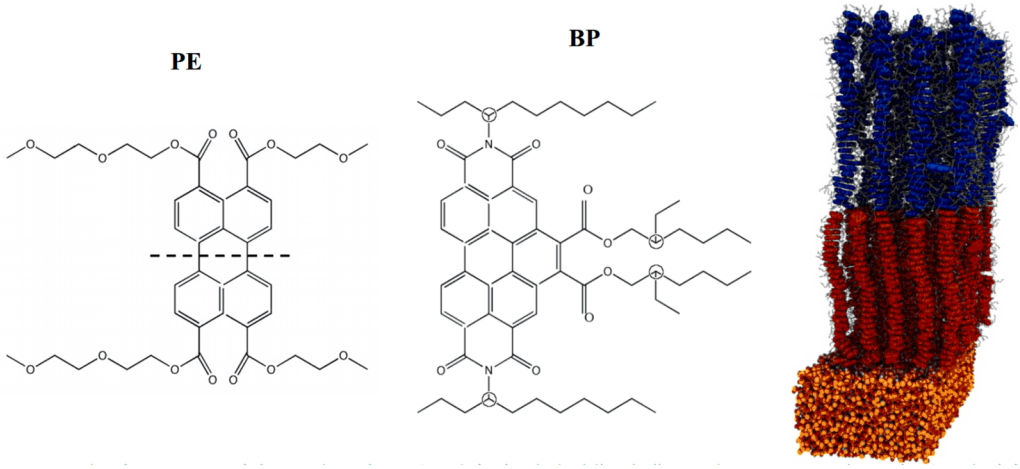

Figure 1. Molecular structures of (left) the perylene donor (PE), where the dashed line indicates the symmetry mirror plane, and (center) the benzoperylene diimido diester acceptor (BP), where circles indicate the chiral centers. (right) Snapshot of the simulated SiO_2/PE/BP stack with highlighted aromatic cores.

chains;[17] (iii) at the same time, the two materials should not be miscible and possibly show antagonistic solubility, in order to form smooth interfaces. These strict requirements have hampered to date the realization of DLC-based OSCs, with the few successful attempts (albeit often showing poor conversion efficiencies) consisting in interfaces between DLCs and crystalline[18−20] or amorphous organic semiconductors[21,22] in either planar- or bulk-heterojunction architectures.

Even if constructing a sharp interface between donor and acceptor DLCs is not a trivial task, this can be achieved as a result of a combination of specific molecular design and careful control of device preparation. The possibility of realizing an oriented bilayer heterojunction of two face-on hexagonal columnar liquid crystals has been recently demonstrated by Thiebaut et al.,[17] who were able to prepare stable bilayers with thicknesses of hundreds of nanometers on glass and on a Si/SiO_2 wafer by subsequent spin-coating deposition of the two components followed by sequential thermal annealing to trigger the macroscopic self-assembly. This result was achieved thanks to a careful design of the molecular features, namely, the antagonistic solubility of the two components resulting from side chains of different lipophilicity, and by the difference in their clearing temperatures, which allowed the sequential annealing. However, both DLC molecules employed in ref 17 presented electron-donor characteristics, hampering the application of that heterojunction to photovoltaics.

The recent synthesis of suitable discotic acceptors achieved by the same group[23] motivated this theoretical study of the planar interface between a perylene donor (PE)[17] and a benzoperylene diimide acceptor (BP)[23,24] (Figure 1). The two materials present robust hexagonal columnar phases at room temperature characterized by nonflowing columns but different transition temperatures; the perylene ester derivative PE possesses polar oxygenated side chains that favor phase separation with compounds bearing conventional apolar alkyl side chains such as BP. In addition, the broad and intense absorption bands of BP[23] and PE,[17] covering large parts of the visible solar spectrum, further favor their possible use in OSC applications. It is worth noticing that obtaining a neat phase separation at the interface between donor and acceptor DLCs should be more difficult than in the case reported in ref 17, as in this case specific charge transfer (CT) interactions may favor complexation and hence intermixing.[25] In view of this possible limitation, other strategies for device preparation that avoid both solvent processing and any passage through isotropic phases seem more promising to the realization of a neat planar heterojunction. An example of a viable strategy would be the vapor deposition of the second component[26] above the previously homeotropically aligned mesophase of the first one.

To achieve a realistic and quantitative theoretical prediction of electronic properties at the interface, idealized models of molecular positions and orientations of donors and acceptors are of limited use.[27,28] It is then worth resorting to atomistic molecular dynamics (MD) simulations, which have been successfully employed to investigate the phase behavior and structural properties of liquid crystals[4,29,30,31] and, when coupled with quantum-mechanical (QM) calculations, to establish the relationships between structure and electronic properties under given thermodynamic conditions.[15,28,30,32,33] On the electronic structure side, organic D−A interfaces have been the subject of different theoretical studies addressing the effects of the environment on the charge transport levels, such as band bending or energetic disorder,[34−39] whose evaluation requires methods capable of describing the polarization of electronic clouds in the medium and accounting for local electric fields, as well as knowledge of the molecular organization.[27] In a very recent work,[34] we used microelectrostatics (ME) and QM calculations based on MD structures to investigate the electron−hole separation energetics at the P3HT−PCBM interface, disclosing the microscopic origin of the high quantum efficiencies measured for this system and demonstrating at the same time the accuracy of this computational approach. Actually, ME is a method mostly suitable for describing electrostatics and polarization at the nanoscale, as it relies on accurate molecular inputs from QM calculations[40] while at the same time being computationally cheap enough to sample electronic properties on the many molecular sites generated in realistic MD simulations.

In the present work, we profited from these recent advances in computational organic electronics by applying a similar methodology to the investigation of the interface between the columnar phases of BP and PE, with the double intent of investigating the morphology of the DLC−DLC interface and

dx.doi.org/10.1021/ja4114769 | J. Am. Chem. Soc. 2014, 136, 2911−2920

understanding the relationship between the molecular organization and the energetics and kinetics of the charge separation processes at the interface between two discotic materials. While in our previous works we focused on the best-characterized systems, such as pentacene/fullerene[27,37] and P3HT/PCBM,[34] this study has instead a predictive character, as it aims to understand the microscopic factors governing the competitive electronic processes taking place at the D−A interface and to devise practical design principles for the engineering of discotic materials for high-quantum-efficiency solar cells. The task is not trivial, as some of the factors that could seem to favor charge dissociation (e.g., face-to-face arrangement of the D and A aromatic cores) could also favor the opposite recombination,[41] leading to an overall outcome on OSC performance that is very difficult to foresee and that we attempt to disclose in the following.

RESULTS AND DISCUSSION

Structures of Columnar Phases and Interfaces. After equilibration at 300 K, both PE and BP bulk samples showed high orientational order, measured as is customary by the order parameter $\langle P_2 \rangle = (3\langle \cos^2 \boldsymbol{u}\cdot\boldsymbol{z}\rangle - 1)/2$, where $\boldsymbol{u}$ is the normal to the aromatic core of the molecule and $\boldsymbol{z}$ is the direction of the column axes: we measured $P_2 = 0.92$ and 0.94 for PE and BP, respectively. These values are consistent with the presence of a columnar phase,[42] and they are accompanied by two-dimensional positional order, as shown by the distribution functions of the intermolecular distances in the xy plane, $g(r_{xy})$ and $g(r_x, r_y)$, which are plotted in Figures 2 and 3, respectively, and were

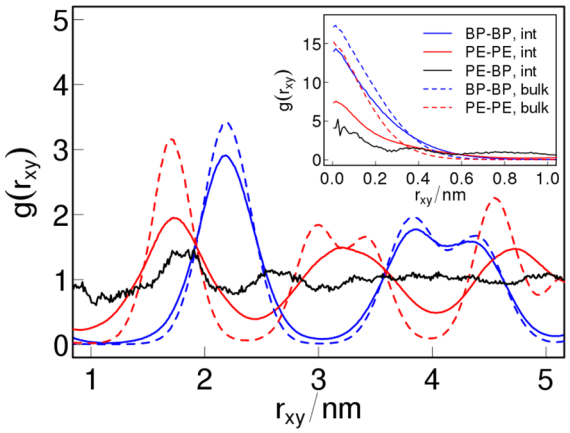

Figure 2. In-plane radial distributions of the intermolecular distances, $g(r_{xy})$, calculated in the bulk (continuous lines) and in the multilayer sample (dashed lines): BP−BP (blue lines); PE−PE (red lines); PE−BP (black line). For the PE−BP case, only molecular pairs in a region within ±10 Å of the interface were used.

calculated using the centers of mass of the aromatic cores of the molecules. The spatial arrangement of the red and blue spots in $g(r_x, r_y)$ indicates that both compounds in their bulk phases possess nearly perfect hexagonal order, and the lattice parameters calculated from the average simulation box sides x and y are in fact very close to the experimental values obtained by X-ray diffraction (the theoretical values are about 17.3 and 22.2 Å for PE and BP and the experimental values about 17.7 and 21.9 Å for PE and BP, respectively[17,23]). The hexagonal order and the value of the lattice spacing a are also confirmed by the typical peaks present in the $g(r_{xy})$ plot: the first peak is well-defined, nearly Gaussian, and positioned at $r_{xy} = a$ (this

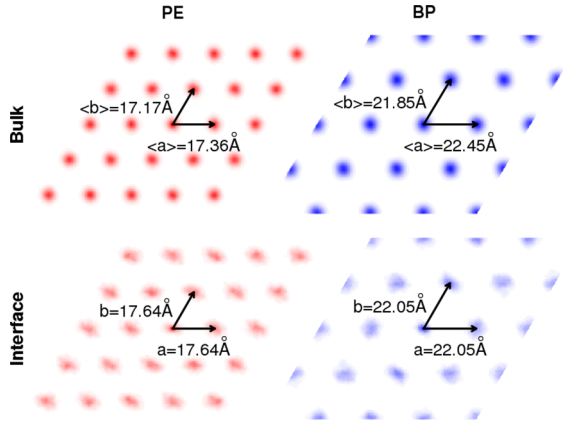

Figure 3. Two-dimensional histograms of the BP−BP (blue) and PE−PE (red) intermolecular distances projected in the xy plane, $g(r_x, r_y)$, calculated in the bulk (top) and in the multilayer sample (bottom).

shape rules out the possibility of a rectangular phase, where a second peak should appear at a distance very close to a), while the second and the third peaks are not completely separated and correspond to $r_{xy} = \sqrt{3}a$ and $r_{xy} = 2a$, respectively. The π-stacking distances were instead estimated from the positions of the first peak of the $g(r_z)$ distributions (not shown), which gave values of 3.53 and 3.56 Å for PE and BP, respectively; these compare well with the experimental value of about 3.5 Å.[17,23]

The agreement between the simulated and experimental lattices provides support for the quality of the force field and for the reliability of the results for the SiO_2/PE/BP multilayer system. The best commensurism between the PE and BP layers was obtained by building a (5×5) supercell of PE layer and a (4×4) supercell of BP. The amorphous SiO_2 support was then built, imposing a hexagonal simulation box with surface vectors of 88.2 Å, to obtain a surface that could accommodate the PE and BP supercells. The choice of a fixed simulation box, although unavoidable if a solid support (SiO_2) is present, implies several limitations to the system degrees of freedom, the most important being that hexagonal translational symmetry is imposed, in practice preventing for instance the rotation of the PE and BP lattices with respect to each other or the formation of phases with lower symmetry. However, some variations are still possible with respect to the bulk, as the lattices can translate from their initial relative positions, the columnar phase can be destabilized, and the orientational order can change at the interfaces because of local lattice deformations. Indeed, partial disruption of the orientational order was observed, as shown by the P_2 versus z profile shown in Figure 4, in particular for PE at the two interfaces with SiO_2 and BP. The positional order of PE, characterized by the density fluctuations along the layer normal (Figure 4 top), exhibits opposite trends at the two interfaces: the order is enhanced close to SiO_2 and lowered at the interface with BP. Conversely, the BP orientational order seems to be unaffected by the presence of the interfaces with PE or vacuum, and BP shows an overall lower density and structuring with respect to PE.

Despite the interfacial effects, we can see from the bidimensional $g(r_x, r_y)$ pattern in Figure 3 that both liquid crystals maintain hexagonal symmetry in the layered sample. Nevertheless, we notice a significant difference with respect to the $g(r_x, r_y)$ pattern calculated in the bulk phases: in the multilayered system the peaks are clearly more diffuse, indicating a decrease in positional order within the columns.

dx.doi.org/10.1021/ja4114769 | J. Am. Chem. Soc. 2014, 136, 2911−2920

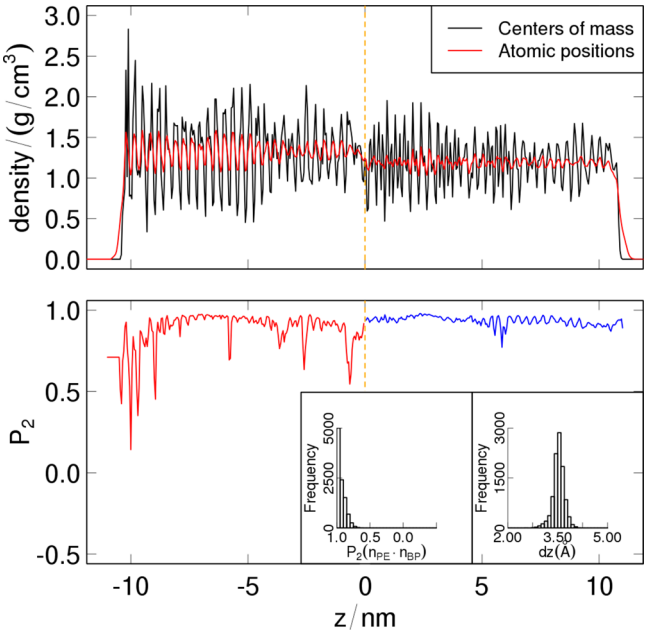

Figure 4. (top) Average density and (bottom) order parameter P_2 as functions of the position z through the BP (blue) and PE (red) layers. The SiO_2 support extends below $z \approx -10$ nm, while vacuum is found for $z \gtrsim 10$ nm. Insets: distributions of (right) the intermolecular distances along z and (left) the order parameter P_2 calculated for the five BP−PE "good matching" molecular pairs lying face-to-face at the D−A interface.

The same conclusion can be drawn by comparing the radial distribution functions $g(r_{xy})$ in Figure 2. Indeed, the decrease in the intensity and the width of the few first peaks of g_{BP-BP} and g_{PE-PE} suggest that molecules belonging to the same column are less aligned in the layered system than in the bulk phase. We also notice that the decrease in the peak intensity is more important for g_{PE-PE} than for g_{BP-BP}, demonstrating that the PE columns are not as well aligned as the BP columns.

We also calculated the mixed BP−PE radial distribution function in a small slice centered at the interface (±10 Å from the interface), again using the intermolecular distances projected in the xy plane (black curve in Figure 2). The presence of a peak at 0 Å in this plot is suggestive of a non-negligible number of BP−PE interfacial pairs having a face-to-face arrangement. We analyzed in detail the couples of BP and PE molecules formed at the interface and found that five BP−PE molecular pairs present a good matching of their aromatic cores, with a stacking distance of less than 6 Å and an in-plane shift of less than 3.5 Å. For these pairs, the distribution of the orientational order parameter P_2 and the distribution of the stacking distance have been calculated and are reported in the insets of Figure 4. The results demonstrate that the molecules are π-stacked at an average distance of 3.6 Å with their cores aligned with the column axes. The number of these good matching couples (5) is non-negligible, as it represents about one-fourth of the total interface considering the number of BP and PE molecules right at the interface (16 and 25, respectively), but it is clearly dependent on the commensurism enforced by the simulation cell and by our initial conditions (one column of PE and BP had identical xy positions in the initial cell, and the six neighboring columns had just a small mismatch equal to the difference between the two lattice parameters, $a_{PB} - a_{PE}$; see Figure S3 in the Supporting Information and Figure 5).

In a real interface between two columnar liquid crystals with a certain difference between their lattice parameters (17.7 and 21.9 Å here), we can expect the number of contiguous D−A columns to be dependent on the lattice mismatch. The question that arises for such a system is whether having such well-matched D and A columns at the interface is beneficial for the performance of a planar-heterojunction OSC. To answer this question, in the remainder of the paper we compare the relevant electronic processes in two limiting situations that may occur at a real planar interface as a consequence of the different lattices of D and A. To this end, the MD simulation was exploited by extracting from our sample two cylindrical clusters that markedly differ in the relative positions of the PE and BP central columns (Figure 5): in the first one, the interface

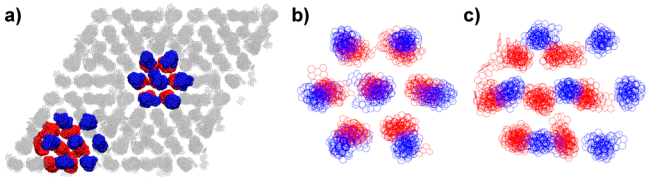

Figure 5. Top view of the cylindrical clusters employed for electronic properties calculations: (a) 2 × 2 replica of the simulated sample, with the selected "good matching" and "bad matching" clusters highlighted; (b, c) zoomed views of (b) the good matching cluster and (c) the bad matching cluster. By "matching" we indicate the relative horizontal displacement of the BP (blue) and PE (red) columns at the D−A interface, with "good" indicating a displacement close to zero (central columns in b) and "bad" a displacement of about half the column−column distance (central columns in c).

between BP and PE consists of molecules with largely superimposed aromatic cores (hereupon termed "good matching"; see Figure 5b), while for the second type there is a rather large horizontal displacement between the BP and PE cores ("bad matching"; see Figure 5c), with each one facing the alkyl chains of the opposite semicolumn.

Energetics of Electron−Hole Separation. The transport energy levels of localized charge carriers in organic semiconductors comprise both intramolecular and intermolecular contributions (the localized charge picture is supported by tight binding calculations; see the Supporting Information for details). In principle, an additional energy level shift may arise across heterojunctions as a result of an interface dipole generated by ground-state CT between D and A molecules. In the specific case of the present BP/PE system, both theoretical calculations and experimental investigations point to negligible CT with no appreciable effect on the energy landscape (see the Supporting Information for details), and therefore, ground-state CT effects are not discussed further here.

The intramolecular part (gas-phase ionization potential, IP_{gas}, for holes and electron affinity, EA_{gas}, for electrons) was evaluated at the AM1 level for molecular geometries extracted from the MD simulations. Actually, IP_{gas} for PE and EA_{gas} for BP do not show any specific trend with the distance from the D−A interface (see Figure S8 in the Supporting Information) but rather exhibit scattered values with standard deviations of ∼0.11 and ∼0.09 eV, respectively. Hence, in the specific case of the PE−BP interface, and unlike interfacial polymeric chains,[34,43] the intramolecular contribution to the transport

dx.doi.org/10.1021/ja4114769 | J. Am. Chem. Soc. 2014, 136, 2911−2920

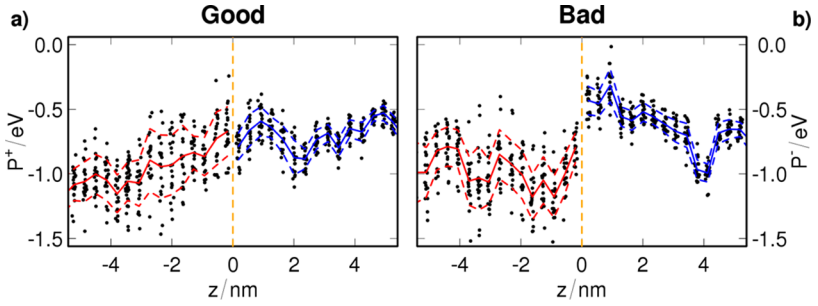

Figure 6. Polarization energies for holes in PE (P^+; time averages and error bars are shown as continuous and dashed red lines) and electrons in BP (P^-; time averages and error bars are shown as blue lines) for molecules extracted from the central columns of cylindrical clusters presenting either (a) good or (b) bad matching at the interface.

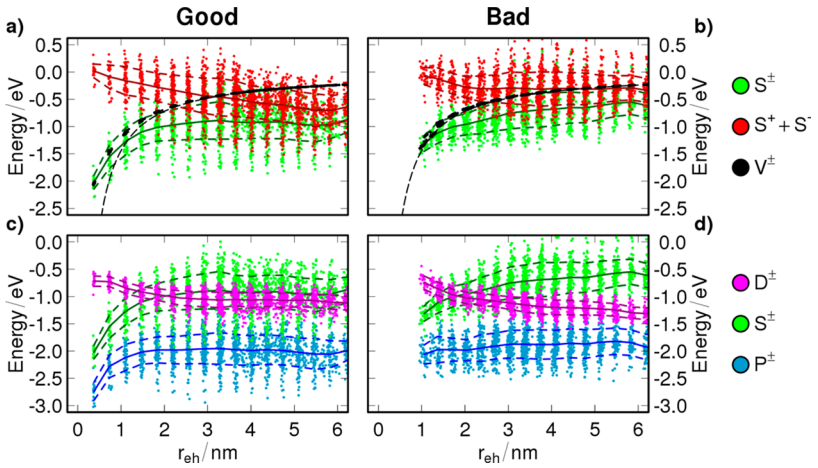

Figure 7. Energy levels for geminate e−h pairs. (a, b) Single-charge static polarization energies (red), Coulomb interactions between the hole and electron charge distributions (black), and their sum (green) for e−h pairs as a function of the e−h distance (r_{eh}) for moving charges along the central column of the cylindrical clusters presenting (a) good or (b) bad matching at the interface. The gray dashed line represents the Coulomb interaction between point unit charges, $-e^2/(4\pi\varepsilon_0 r_{eh})$. (c, d) The corresponding total (blue), static (green), and dynamic (magenta) polarization energies for (c) good or (d) bad matching.

levels does not have a net effect on the e−h separation but represents only a source of energetic disorder.

Profiles of the polarization energies for single holes in PE (P^+) and electrons in BP (P^-) at the good and bad matching geometries are shown in Figure 6. The energy landscape is governed by electrostatic interactions between permanent atomic charges (see Figure S9 in the Supporting Information), which contribute to a large extent to the energetic disorder in both time (different values at different times) and space (different average values upon moving from one molecule to another). This disorder is mainly caused by the interactions of each molecule with the polar groups on flexible side chains belonging to molecules in adjacent columns, and it is in fact greatly reduced in ME calculations performed on the sole central column of the clusters. Its magnitude for BP (σ_{P^-} = 0.13 eV) is consistent with experimental measurements for hexasubstituted triphenylene DLCs bearing polar groups in the side chains (0.087−0.127 eV),[44] while it is twice as big on the PE side (σ_{P^+} = 0.22 eV) because of the larger number of carbonyls and ethers. Despite the rather noisy profiles, in Figure 6 some net trends can also be noticed, as the decrease of P^+ and P^- with the distance from the interface in the case of good and bad matching columns, respectively. Ideally, summing up the effects for holes and electrons, it is easy to conjecture a certain stabilization effect (more negative polarization energies) for charges localized far away from the interface.

To quantify this effect, we must then consider the polarization energy for a geminate e−h pair present in the system, rather than limiting ourselves to individual charges, as shown in Figure 7. The static contribution to these energies is plotted in panels a) and b) for the good and bad matching interfaces. The total electrostatic energy of e−h pairs (green dots) can be partitioned into a contribution from single-charge energy levels (S^++ S^-; red dots) plus the interaction between the excess charge distributions of the hole and the electron ($V^{\pm}$; black dots).[34] The term "excess charge distribution" refers here to the set of atomic charges obtained as the difference between that of the (positively or negatively) charged molecule and that of the neutral molecule. As hinted above, the energy levels for single charges favor, on average, the separation of e−h pairs at both of the interfaces, while $V^{\pm}$ is always attractive and constitutes the energetic barrier that must be overcome to obtain free charge carriers. However, the value of the binding energy $V^{\pm}$ for e−h pairs at the shortest distance is almost 1 eV smaller in magnitude in the case of bad matching (Figure 7b) than in the case of good matching (Figure 7a) as a direct consequence of the larger intermolecular distance between the aromatic cores of BP and PE. As a matter of fact, bad matching of columns of D and A molecules results in loosely bound e−h pairs (formed upon exciton dissociation), which are more likely to separate.

dx.doi.org/10.1021/ja4114769 | J. Am. Chem. Soc. 2014, 136, 2911−2920

The dynamic polarization energies of e−h pairs are shown as magenta dots in Figure 7c,d. This contribution is due to induced dipoles in the medium and provides a further driving force for charge dissociation of comparable magnitude (∼0.5 eV of energy stabilization) for the two interfaces. This effect is rather general and is due to the larger stabilization by means of the polarizable environment experienced by the two well-separated monopoles with respect to the case of a closely located e−h pair, which is rather akin to a point dipole. A comparable decrease in dynamic e−h polarization energy has in fact been calculated for the P3HT−PCBM interface.[34] Despite their nearly identical dynamic polarization profiles, the total e−h polarization energies (blue dots) are strikingly different for the good and bad matching clusters: in the first case (Figure 7c), e−h pairs have to overcome an energy barrier of ∼0.8 eV within a distance of 2 nm before they reach a flat (on average) yet rough energy landscape and produce two free charge carriers. On the contrary, in the case of bad matching, the lower e−h binding energy gives rise to a flat energy landscape already from the initial steps of charge separation.

Electron−hole polarization energies calculated along the trajectory for the two cases of interest were used to make a statistical assessment of the energetically favorable pathways for charge separation, as defined in ref 34. Figure 8a,b shows the

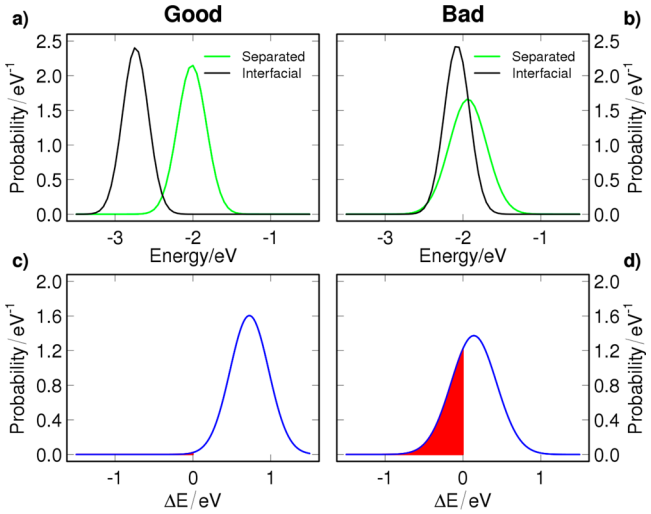

Figure 8. (a, b) Probability distributions of polarization energy for interfacial (r_{eh} < 5 Å and r_{eh} < 13 Å for the good and bad matching cases, respectively; black lines) and separated (r_{eh} > 59 Å; green lines) e−h pairs for the clusters presenting (a) good and (b) bad matching at the interface. (c, d) Distributions of energy differences between separated and interfacial e−h pairs for the cylindrical clusters presenting (c) good and (d) bad matching at the interface. The red-shaded areas show the fractions of barrierless (ΔE < 0) e−h separation events: 0.2% in (c) and 30.9% in (d).

distributions of polarization energies for interfacial (black lines) and free (green lines) e−h pairs, assumed to be Gaussian with mean values and standard deviations calculated from the ME results. The two distributions largely overlap in the case of bad matching (panel b), while for good matching (panel a) the superposition is limited to a small portion of the tails of the relative distributions. Figure 8c,d shows instead the probability distribution of the difference between the interfacial and separated-charge energy levels obtained under the reasonable hypothesis of statistical independence between the two situations. The fraction of e−h pairs that can separate without energy expense, as measured by the area subtended by the energy difference distribution for ΔE < 0 (red-shaded regions in Figure 8c,d), amounts to 31% for the bad matching case (panel d) and is negligible for the good matching one (panel c). Interestingly, this shows that charge sweep-out and collection[41] can occur also in the absence of an external bias, which is not included in our energy picture.

The beneficial effects of weaker e−h binding due to larger distances between the D and A units was demonstrated by Holcombe et al.[45] In that work, increases in the OSC photocurrent and efficiency upon introduction of bulky side groups in polythiophenes interfaced with several electron acceptors were reported. Here we provide a further theoretical confirmation of this concept based on a proper evaluation of electrostatic and polarization effects in realistic model interfaces, showing that lattice mismatch offers a viable opportunity for its practical implementation in one-dimensional semiconductors.

Kinetics of Electronic Processes. The performance of OSCs is governed not only by the energetics of e−h separation but also by the kinetics of the different, and in some cases competitive, electronic processes taking place at the D−A interface, such as h/e transfer along the respective columns, exciton dissociation (ED), and charge recombination (CR). To rationalize the kinetics of these processes, one must take into account the electronic couplings as well as the sometimes counterintuitive results of electron transfer theories, as the so-called Marcus inverted regime, where the rate decreases with the energy gained in the CT process.[46] For this purpose, we relied on a hopping picture based on the Marcus−Levich−Jortner (MLJ) model[47,48](see eq 1 in Computational Details), whose applicability to our case was confirmed by tight binding calculations showing that energetic disorder leads to localized charge carriers over single molecular units (see the Supporting Information for details). The strong localization scenario in this system suggests that charge separation occurs through consecutive hops, ruling out long-range coherent processes as proposed by Troisi and co-workers for fullerene/polymer heterojunctions.[39,43]

We first consider ED, which should occur within the exciton lifetime in order to achieve quantitative photocarrier generation. The reported experimental lifetimes for perylene tetracarboxylic dianhydrides are on the order of hundreds of picoseconds in thin films[49] and even larger for perylene bisimides in columnar aggregates in solution.[50,51] Hence, ED rates must be larger than 10^9 s^{-1} to ensure efficient dissociation. This is certainly the case for the good matching arrangement (green symbols in Figure 9a,c), while for the bad matching case the larger distance between D and A reduces the electronic couplings to tenths of meV (see Figure 10d and Table S6 in the Supporting Information), lowering the rates to values comparable to those for exciton decay. Besides, the energy gap between the excited state (DA* or D*A) and the D^+A^- state is quite small for the bad matching case, with CT occurring near the crossover between the direct and inverse Marcus regimes,[52] therefore meeting the condition for the highest possible rate (for a given value of other parameters). This makes the ED rates very sensitive to our estimates for the external (or intermolecular) reorganization energy (λ_{ext}) and the lowest singlet excitation energy ($\Delta^{S_1-S_0}$) and more importantly to small chemical modifications of the D and A molecules.[45] To ensure the internal consistency of the

dx.doi.org/10.1021/ja4114769 | J. Am. Chem. Soc. 2014, 136, 2911−2920

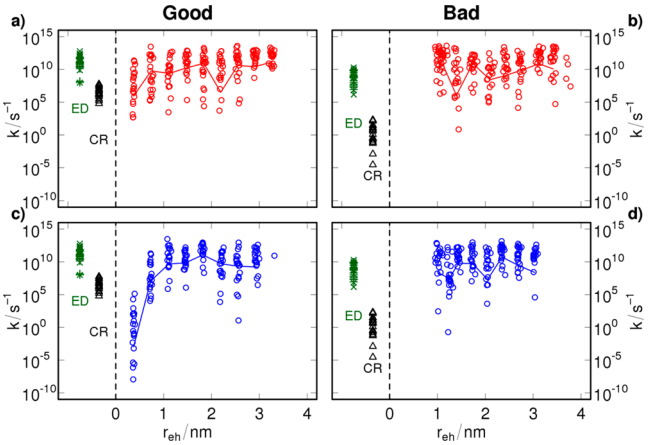

Figure 9. CT rates for holes in PE (red circles/line in a, b) and electrons in BP (blue circles/line in c, d) hopping away from the interface along the central column while the geminate charge is fixed at the interfacial site in the other material. Results for the good and bad matching columns are shown in the left and right panels, respectively. Circles show the rates calculated for different frames along the MD trajectory (static limit), while lines show rates calculated with mean transfer integrals and mean site energies (dynamic limit[53]). Green symbols correspond to exciton dissociation (ED) rates (crosses for D*A and plus signs for DA*) and black triangles to charge recombination (CR) rates, calculated for BP/PE dimers at the (a, c) good and (b, d) bad matching interfaces. For clarity, the CR and ED rates are plotted at arbitrary r_{eh} values.

computational approach, we used CI/AM1 excitation energies, which are in semiquantitative agreement with experimental data: the computed $\Delta^{S_1-S_0}$ values are 2.9 and 3.1 eV (averages over 20 geometries from the MD trajectory), compared to the experimental 0−0 optical transitions in columnar phases of 2.5 and 2.8 eV for PE[17] and BP,[23] respectively.

Turning to the competition between the e−h separation and the CR process, Figure 9 shows the CT rates for moving an electron (hole) away from the interface along the BP (PE) central column while fixing one hole (electron) in the first PE (BP) molecule at the interface. In the case of good matching columns, the limiting step for holes (red circles in Figure 9a) and electrons (blue circles in Figure 9c) is represented by the first hop from the molecule at the interface to its neighbor in the same column. The continuous lines show the rates calculated with transfer integrals and site energy differences averaged over the MD trajectory (the so-called "dynamic limit"[32,53]), which for the first steps of e−h separation are lower than 1 s^{-1}, or in other words not possible in the time window of our simulation. The rates for both holes and electrons reach a plateau within 2−3 hops, in correspondence with the plateau in polarization energies visible in Figure 7c, attaining a value of about 10^{10} s^{-1}. Conversely, in the case of bad matching, the transfer rates for holes (red circles in Figure 9b) and electrons (blue circles in Figure 9d) oscillate around 10^{10} s^{-1} already from the first steps of charge separation. The faster e−h separation in the bad matching case is a direct consequence of the barrierless energy profile in Figure 7d, as minimal differences between the intracolumn CT integrals for the good and bad matching columns are observed (Figures S6 and S7 in the Supporting Information). Moreover, the values of the e/h rates far from the interface are the same for the two cases considered and independent of the presence of the geminate charge at the interface, as confirmed by comparison with the single-charge transfer rates in Figure S10 in the Supporting Information. It is worth noticing that the rates between the same couple of molecules may vary by orders of magnitude on the nanosecond time scale and thus that every site may behave as a dynamic trap for charge carriers, as is well-known for one-dimensional structures[54] and in particular for DLC systems.[32,53]

The CR kinetics is also strikingly different in the two cases, with rates on the order of 10^7 and 10^1 s^{-1} for the good and bad matching cases, respectively (black triangles in Figure 9). CR therefore competes with e−h separation in the good matching case but is not a limiting process for charges moving through bad matching columns. The much lower CR rates in the bad matching case with respect to the good matching one are due mainly to the difference in the electronic couplings but also to the larger energy released when D and A aromatic cores are not closely stacked (see Figure 10d), which decreases the rate as the process takes place in the Marcus inverted regime.

CONCLUSIONS

We have reported the first theoretical investigation of a planar interface between electron D and A discotic liquid crystals, addressing the relationship between morphology and functionality in an ideal planar-heterojunction solar cell by means of a multiscale modeling approach including atomistic molecular dynamics, quantum-chemical, and microelectrostatic calculations.

At the interface between two columnar discotic liquid crystals with different lattice constants oriented homeotropically, several possibilities for the matching of D and A columns are found, corresponding to different pathways for the separation of photoinduced e−h pairs through one-dimensional transport along the columns. By considering the two limiting cases of almost perfectly and barely matching D and A columns, our modeling shows that, quite surprisingly, column mismatch has a favorable effect on the e−h separation process. The key element for this result is the different contribution from e−h electrostatic interactions to the energy of interfacial D^+A^- states in the good and bad matching cases, which can be traced back to the different distances between facing D and A molecules. In fact, qualitatively different energy profiles for e−h separation are observed in the two cases: for good matching columns the e−h separation requires overcoming an activation barrier of ∼0.8 eV, while in the bad matching case the e−h separation is, on average, a barrierless process. These dissimilar energy landscapes, along with the very different electronic couplings between interfacial D and A molecules in the two scenarios, give rise to strikingly different kinetics for the electronic processes.

Our main findings are summarized in Figure 10, where we show ensemble-averaged energies, couplings, and resulting rates for the relevant processes. The weaker binding between geminate charges in the bad matching columns results in high rates for hole and electron transfer away from the interface already from the first steps of charge separation, which instead constitutes the bottleneck for e−h separation in the good matching case (Figure 10a,b). At the same time, we found that the ground-state recombination of interfacial e−h pairs (Figure 10c) competes with charge separation, providing a channel for energy loss. Conversely, in bad matching columns, the smaller electronic couplings and also the less stable D^+A^- state make CR many orders of magnitude slower than e−h separation. However, an efficient OSC requires fast exciton dissociation prior to charge separation. The weak D−A couplings in the

dx.doi.org/10.1021/ja4114769 | J. Am. Chem. Soc. 2014, 136, 2911−2920

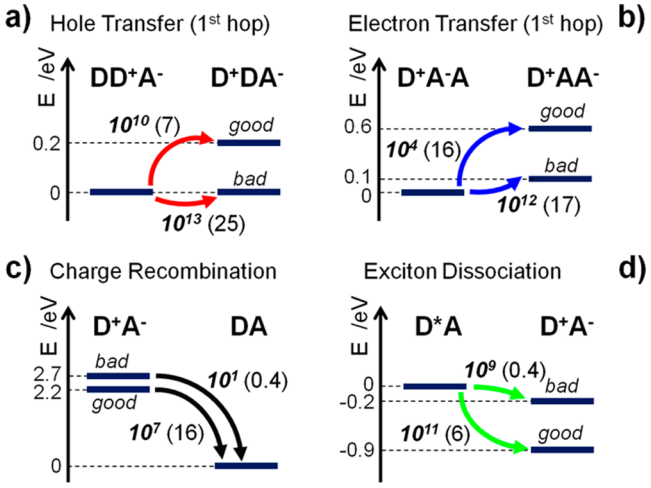

Figure 10. Schematic representation of the charge transfer processes occurring at the D−A interface between two columnar liquid crystals. The mean energies of the initial (left in each scheme) and final (right) states, mean absolute values of the relevant electronic couplings (in meV, shown in parentheses), and rates (order of magnitude in s^{-1}, shown in bold italic type) are shown for the cases of good and bad matching columns. ED from the DA* state is qualitatively similar to that shown in (d), with energy differences of −0.9 and −0.4 eV, rates of 10^{12} and 10^{9} s^{-1}, and couplings of 34 and 0.5 meV in the good and bad matching cases, respectively.

case of (very) bad matching columns lead to ED rates that are 2 orders of magnitude smaller than in the good matching case, although still acceptable in terms of absolute values (~10^{9} s^{-1}).

Though the quantitative results reported above are specific to our case study, namely, the BP−PE interface, they provide some general design principles for the realization of organic solar cells based on discotic liquid crystals. First, it turns out that interfaces between D and A materials with very similar columnar phase lattices should be avoided in order to minimize the energy losses due to fast charge recombination at π-stacked D−A pairs. On the other hand, lattice mismatch leads to faster charge separation and slower recombination, but it negatively affects exciton dissociation because it reduces the coupling between their π-conjugated electron densities. As a consequence, to fully exploit the potential of DLCs in solar cells, the lattice mismatch must be engineered, for instance by modulating the length of the side chains. Overall, this study suggests that contrary to conventional wisdom, the interfacial mismatch between π-conjugated cores of mesogens is an important design principle rather than a situation to be avoided, as it favors the formation of weakly bound CT states that can efficiently mediate charge separation without being prone to fast recombination.

COMPUTATIONAL DETAILS

Molecular Dynamics Simulations. In order to mimic a typical experimental setup, we constructed our interface by stacking BP and PE columnar phases oriented homeotropically on top of a silica slab (Figure 1 right). The construction of such a multilayer system is rather complex from the computational point of view because it requires several simulation steps. First, a force field apt to reproduce correctly the lattice parameters and structures of both compounds was parametrized. We started with the AMBER united atom (UA) force field[55] and adjusted stretching and bending parameters to reproduce B3LYP/cc-pVTZ equilibrium structures of the isolated molecules; the force field was completed with torsional potentials and UA point charges obtained at the quantum-chemical level (see the Supporting Information for details). This procedure has proved to be successful in several recent studies of DLCs.[53,56]

The next step consisted of reproducing the morphologies of the two liquid crystals. We carried out MD simulations in the *NpT* ensemble (T = 300 K, p = 1 bar) of the columnar BP and PE bulk phases, allowing the box sides and angles to change independently to adapt to the symmetry of the columnar phase. The samples studied were constructed as 4 × 4 and 5 × 5 supercells for BP and PE, respectively (see the Supporting Information for further details). Equilibration and production phases of 50 ns each were performed, monitoring the convergence of the cell parameters and total energy to constant average values. All of the simulations were carried out with the open-source code NAMD.[57]

The third step was the preparation of an amorphous silicon oxide slab. First, a bulk monoclinic cell with sides corresponding to the BP cell and thickness z adjusted to achieve the experimental density of vitreous silica at room temperature was equilibrated with LAMMPS[58] according to the procedure described in ref 59 using the Du−Cormack force field.[60] Then a slab was obtained by removing the boundary conditions of the simulation box in one direction, as described in ref 31. In order to increase the roughness to realistic values of the otherwise atomically flat surface, outer SiO_2 units were randomly picked and removed from the slab surface. The creation of these defects was followed by thermal annealing at 900 K (1 ns) and subsequent cooling to 300 K at a rate of 5 K/ps. The surface was then hydrated by capping unsaturated O and Si atoms with H and OH groups, respectively. The resulting structure was finally minimized at 0 K, achieving a roughness of about 2 Å. To reduce the computational effort, only a thin layer (~10 Å) of atoms on top of the silica surface was set free to move, while the remaining atoms were kept fixed during the subsequent MD simulations. The interactions between SiO_2 and organics were modeled with the Clay force field.[61] Once the three layers (SiO_2, PE, and BP) were independently prepared, the PE (donor) layer (11 nm) and the BP (acceptor) layer (11 nm) were stacked on top of the silica slab (7 nm) to produce the starting configuration for the planar-heterojunction simulation. The BP−air interface was modeled by adding an empty space of about 20 nm to the simulation box. The whole system was equilibrated for 30 ns, followed by 30 ns of production, with an *NVT* ensemble MD simulation carried out with NAMD at room temperature (T = 300 K).

Electronic Properties Calculations. In this work we considered different CT processes occurring at the D−A interface, namely, exciton dissociation (...DD*AA... or ...DDA*A... → ...DD$^+$A$^-$A...), hole transfer (...DD$^+$... → ...D$^+$D...) and electron transfer (...A$^-$A... → ...AA$^-$...) within the same material, and charge recombination at the interface (...DD$^+$A$^-$A... → ...DDAA ...). Our analysis relied on the Marcus−Levich−Jortner theory for nonadiabatic intermolecular electron transfer, with the electronic properties of interest all appearing in the well-known MLJ rate expression:[47,48]

$$k = \frac{2\pi}{\hbar} t^2 \sqrt{\frac{1}{4\pi\lambda_{ext} k_B T}} \sum_{n=0}^{\infty} \left\{ \exp(-S_{eff}) \times \frac{S_{eff}^{\,n}}{n!} \exp\left[-\frac{(\Delta E + \lambda_{ext} + n\hbar\omega_{eff})^2}{4\lambda_{ext} k_B T} \right] \right\} \quad (1)$$

where k is the CT rate constant; ΔE is the energy difference between the initial and final electronic states involved in the CT process and t is the electronic coupling between them; $S_{eff} = \lambda_{int}/\hbar\omega_{eff}$ is the Huang−Rhys factor measuring the strength of electron−phonon coupling, which is directly related to the internal (or intramolecular) reorganization energy (λ_{int}) and to the frequency of the effective vibrational mode assisting the process (ω_{eff}); λ_{ext} is the external (or intermolecular) reorganization energy; and k_B is Boltzmann's constant.

On the basis of B3LYP/cc-pVDZ calculations (see the Supporting Information for details), the values of λ_{int} for the different CT processes were estimated to be λ^{hT} = 0.159 eV, λ^{eT} = 0.247 eV, λ^{CR} = 0.203 eV, $\lambda^{ED,D*}$ = 0.198 eV, and $\lambda^{ED,A*}$ = 0.131 eV. $\hbar\omega_{eff}$ was set to 0.2 eV, a typical value for the energy of the breathing mode of aromatic cores, while λ_{ext} was set to 0.2 eV, a usual value for disordered

dx.doi.org/10.1021/ja4114769 | J. Am. Chem. Soc. 2014, 136, 2911−2920

materials.[32,53] Finally, the temperature was set to 300 K, as in the MD simulation. The robustness of our results with respect to possible inaccuracies in the reorganization energy values was explicitly verified, with the average rates discussed throughout this article changing by less than 1 order of magnitude when λ_{int} and λ_{ext} were varied by ±0.1 eV. Although the external reorganization energy might depend on the specific molecular environment and hence on the distance from the interface or on the interface matching, a constant value of λ_{ext} was assumed here because of the intrinsic difficulties in the microscopic evaluation of this quantity.[62,63] Electronic couplings were computed at the valence-bond/Hartree−Fock (VB/HF) level of theory.[64] In the VB/HF scheme, the wave function of a set of mutually interacting molecules, described at the semiempirical HF-AM1 level, is expressed as a combination of pertinent charge-localized states (VB states) and determined through a self-consistent procedure. Electronic couplings were calculated for couples of molecules at the MD simulation geometry as $t^- = \langle A^-A|\hat{H}|AA^-\rangle$ for electron transfer, $t^+ = \langle D^+D|\hat{H}|DD^+\rangle$ for hole transfer, and $t^{CR} = \langle D^+A^-|\hat{H}|DA\rangle$ for charge recombination. The ED couplings $t^{ED,D^*} = \langle D^*A|\hat{H}|D^+A^-\rangle$ and $t^{ED,A^*} = \langle DA^*|\hat{H}|D^+A^-\rangle$ were calculated at the AM1 level as one-electron transfer integrals between relevant frontier orbitals:[65] $t^{ED,D^*} = \langle LUMO_D|\hat{H}|LUMO_A\rangle$ and $t^{ED,A^*} = \langle HOMO_D|\hat{H}|HOMO_A\rangle$. The energies of the states involved in the CT processes are expressed as follows:

$$E_i^+ = IP_i^{gas} + P_i^+ \quad (2)$$

$$E_i^- = -EA_i^{gas} + P_i^- \quad (3)$$

$$E_i^* = \Delta_i^{S_1-S_0} + P_i^* \quad (4)$$

$$E_{ij}^{\pm} = IP_i^{gas} - EA_j^{gas} + P_{ij}^{\pm} \quad (5)$$

where E_i^+, E_i^-, and E_i^* are the energies of a hole, an electron, and a singlet exciton at site i, respectively, while $E_{ij}^{\pm}$ is the energy of an e−h pair with the hole at site i and the electron at site j. The energies of such states include *intramolecular terms*, namely, the gas-phase ionization potential (IP_i^{gas}) and electron affinity (EA_i^{gas}), which were evaluated at the restricted HF/AM1 level at the specific geometry of the ith molecule, and the lowest singlet excitation energy ($\Delta_i^{S_1-S_0}$), which was calculated at the CI/AM1 level. To perform electronic structure calculations on UA MD structures, hydrogen atoms were added according to geometrical criteria as in previous works.[4,34,53] The polarization energies for holes (P_i^+), electrons (P_i^-), and e−h pairs ($P_{ij}^{\pm}$), which represent the energy contributions due to *electrostatic interactions with the polarized environment*, were evaluated with classical microelectrostatics (ME) assuming the charges to be localized on individual molecular units. The environmental contribution to the exciton energy was neglected here (P_i^*=0), as this is a higher-order effect with respect to those related to charged species. In practice, excited and ground-state molecules are assumed to be equivalent from the electrostatic point of view.

Microelectrostatic Calculations. Polarization energies were calculated with the ME model based on permanent atomic charges and anisotropic polarizable points (induced dipoles) as described in ref 34. B3LYP/cc-pVDZ ESP-UA charges and polarizable points were placed only on heavy atoms. We calculated the polarizabilities for the aromatic core and the whole molecule separately (see Table S3 in the Supporting Information), and we distributed the core polarizability to the respective atoms in order to fully account for its anisotropy. The difference between the isotropic polarizability of the whole molecule and that of the core was then assigned to side chains. Polarizabilities were distributed proportionally to the atomic numbers of heavy atoms. The polarization energy of a specific charge configuration was computed as the energy difference between the charged and neutral systems: $P^x = U^x - U^0$, where x = +, −, or ± . The energy in the ME model is calculated as a sum over the whole system:[40,66]

$$U = \frac{1}{2}\sum_k (q_k V_k^0 + \boldsymbol{\mu}_k \cdot \mathbf{F}_k^0) \quad (6)$$

where q_k and $\boldsymbol{\mu}_k$ are the permanent charge and induced dipole, respectively, at atomic site k and V_k^0 and $\mathbf{F}_k^0$ are the electric potential and electric field, respectively, at the same site due to permanent charges only (the superscript 0 indicates $\boldsymbol{\mu}_k = 0$). Induced dipoles were calculated in the self-consistent electric field of charges and dipoles themselves ($\mathbf{F}_k$) through an iterative solution as $\boldsymbol{\mu}_k = \underline{\boldsymbol{\alpha}}\mathbf{F}_k$, where $\underline{\boldsymbol{\alpha}}$ is the site polarizability tensor. The polarization energy P^x of a given charge configuration x includes electrostatic and dynamic polarization contributions:[34,64] $P^x = S^x + D^x$. The electrostatic contribution S^x was calculated as the interaction between permanent charges ($\boldsymbol{\mu}_k = 0$), while the dynamic contribution D^x was obtained as the difference between P^x and S^x.

ME calculations were performed on clusters of cylindrical shape with the central axis perpendicular to the interface normal that were extracted from the whole system, for a total of 20 different cluster geometries sampled every 1.5 ns in the production MD trajectory. The clusters included seven columns of 30 molecules per species and extended across the whole sample (see Figure 5). Charges were allowed to move only in the central column, while the six nearest-neighbor columns provided the local polarizable environment for charge motion.

■ ASSOCIATED CONTENT

Supporting Information

Description of force field derivation and cell preparation details, description of calculation of reorganization energies, transfer integral maps for dimers, tight binding calculations, discussion on interfacial charge transfer states. Additional figures and tables. This material is available free of charge via the Internet at http://pubs.acs.org.

■ AUTHOR INFORMATION

Corresponding Author

Gabriele.Davino@gmail.com

Present Address

[#]G.D.: Institut de Physique, Université de Liège, Allée du 6 Août 17, B-4000 Liège, Belgium.

Notes

The authors declare no competing financial interest.

■ ACKNOWLEDGMENTS

The research leading to these results received funding from the European Commission Seventh Framework Programme (FP7/2007-2013) under Grant Agreement 228424, Project MINOTOR. J.I. acknowledges the HPC-Europa2 Transnational Access Programme for funding his collaborative research visits in Bologna and granting access to high-performance computing resources at CINECA and thanks the contributors to the R-Project, a language and environment for statistical computing (http://www.R-project.org/), which he extensively used in processing and analyzing data. Calculations performed in Bordeaux were carried out on mainframe computers of the "Mesocentre de Calcul Intensif Aquitain" (MCIA) financed by Conseil Régional d'Aquitaine and the French Ministry of Research and Technology, with the technical assistance of P. Aurel. The work in Mons was supported by the Région Wallonne OPTI2MAT Program of Excellence, the Interuniversity Attraction Pole Programs of the Belgian Federal Science Policy Office (PAI 6/27 and 7/05), and FNRS-FRFC. Y.O., J.C., and D.B. are research fellows of the Belgian F.R.S.-FNRS.

■ REFERENCES

(1) Markov, D. E.; Tanase, C.; Blom, P. W. M.; Wildeman, J. *Phys. Rev. B* **2005**, *72*, 045217.

(2) Lunt, R.; Benziger, J. B.; Forrest, S. R. *Adv. Mater.* **2010**, *22*, 1233−1236.
(3) Cisse, L.; Destruel, P.; Archambeau, S.; Seguy, I.; Jolinat, P.; Bock, H.; Grelet, E. *Chem. Phys. Lett.* **2009**, *476*, 89−91.
(4) Papadopoulos, T. A.; Muccioli, L.; Athanasopoulos, S.; Walker, A. B.; Zannoni, C.; Beljonne, D. *Chem. Sci.* **2011**, *2*, 1025−1032.
(5) Markovitsi, D.; Marguet, S.; Bondkowski, J. *J. Phys. Chem. B* **2001**, *105*, 1299−1306.
(6) Heremans, P.; Cheyns, D.; Rand, B. P. *Acc. Chem. Res.* **2009**, *42*, 1740−1747.
(7) O'Neill, M.; Kelly, S. M. *Adv. Mater.* **2011**, *23*, 566−584.
(8) Markovitsi, D. *Mol. Cryst. Liq. Cryst.* **2003**, *397*, 89−98.
(9) Sergeyev, S.; Pisula, W.; Geerts, Y. H. *Chem. Soc. Rev.* **2007**, *36*, 1902−1929.
(10) Kaafarani, B. R. *Chem. Mater.* **2011**, *23*, 378−396.
(11) Leight, K. R.; Esarey, B. E.; Murray, A. E.; Reczek, J. J. *Chem. Mater.* **2012**, *24*, 3318−3328.
(12) Laschat, S.; Baro, A.; Steinke, N.; Giesselmann, F.; Haegele, C.; Scalia, G.; Judele, R.; Kapatsina, E.; Sauer, S.; Schreivogel, A.; Tosoni, M. *Angew. Chem., Int. Ed.* **2007**, *46*, 4832−4887.
(13) Bushby, R. J.; Kawata, K. *Liq. Cryst.* **2011**, *38*, 1415−1426.
(14) Sergeyev, S.; Debever, O.; Pouzet, E.; Geerts, Y. H. *J. Mater. Chem.* **2007**, *17*, 3002−3007.
(15) Feng, X. L.; Marcon, V.; Pisula, W.; Hansen, M. R.; Kirkpatrick, J.; Grozema, F.; Andrienko, D.; Kremer, K.; Müllen, K. *Nat. Mater.* **2009**, *8*, 421−426.
(16) Schweicher, G.; Gbabode, G.; Quist, F.; Debever, O.; Dumont, N.; Sergeyev, S.; Geerts, Y. H. *Chem. Mater.* **2009**, *21*, 5867−5874.
(17) Thiebaut, O.; Bock, H.; Grelet, E. *J. Am. Chem. Soc.* **2010**, *132*, 6886−6887.
(18) Schuenemann, C.; Petrich, A.; Schulze, R.; Wynands, D.; Meiss, J.; Hein, M. P.; Jankowski, J.; Elschner, C.; Alex, J.; Hummert, M.; Eichhorn, K.-J.; Leo, K.; Riede, M. *Org. Electron.* **2013**, *14*, 1704−1714.
(19) Sun, Q.; Dai, L.; Zhou, X.; Li, L.; Li, Q. *Appl. Phys. Lett.* **2007**, *91*, No. 253505.
(20) Schmidt-Mende, L.; Fechtenkötter, A.; Müllen, K.; Moons, E.; Friend, R. H.; MacKenzie, J. D. *Science* **2001**, *293*, 1119−1122.
(21) Jurow, M. J.; Hageman, B. A.; DiMasi, E.; Nam, C.-Y.; Pabon, C.; Black, C. T.; Drain, C. M. *J. Mater. Chem. A* **2013**, *1*, 1557−1565.
(22) Dao, Q. D.; Hori, T.; Fukumura, K.; Masuda, T.; Kamikado, T.; Fujii, A.; Shimizu, Y.; Ozaki, M. *Appl. Phys. Lett.* **2012**, *101*, No. 263301.
(23) Kelber, J.; Achard, M.-F.; Garreau-de Bonneval, B.; Bock, H. *Chem.—Eur. J.* **2011**, *17*, 8145−8155.
(24) Eccher, J.; Faria, G. C.; Bock, H.; von Seggern, H.; Bechtold, I. H. *ACS Appl. Mater. Interfaces* **2013**, *5*, 11935−11943.
(25) Zucchi, G.; Viville, P.; Donnio, B.; Vlad, A.; Melinte, S.; Mondeshki, M.; Graf, R.; Spiess, H. W.; Geerts, Y. H.; Lazzaroni, R. *J. Phys. Chem. B* **2009**, *113*, 5448−5457.
(26) Brunet, T.; Thiebaut, O.; Charlet, É.; Bock, H.; Kelber, J.; Grelet, É. *Europhys. Lett.* **2001**, *93*, No. 16004.
(27) Cornil, J.; Verlaak, S.; Martinelli, N.; Mityashin, A.; Olivier, Y.; Van Regemorter, T.; D'Avino, G.; Muccioli, L.; Zannoni, C.; Castet, F.; Beljonne, D.; Heremans, P. *Acc. Chem. Res.* **2013**, *46*, 434−443.
(28) Beljonne, D.; Cornil, J.; Muccioli, L.; Zannoni, C.; Brédas, J.-L.; Castet, F. *Chem. Mater.* **2011**, *23*, 591−609.
(29) Yan, F.; Earl, D. J. *J. Chem. Phys.* **2012**, *136*, No. 124506.
(30) Schrader, M.; Körner, C.; Elschner, C.; Andrienko, D. *J. Mater. Chem.* **2012**, *22*, 22258−22264.
(31) Roscioni, O. M.; Muccioli, L.; Della Valle, R. G.; Pizzirusso, A.; Ricci, M.; Zannoni, C. *Langmuir* **2013**, *29*, 8950−8958.
(32) Idé, J.; Méreau, R.; Ducasse, L.; Castet, F.; Olivier, Y.; Martinelli, N.; Cornil, J.; Beljonne, D. *J. Phys. Chem. B* **2011**, *115*, 5593−5603.
(33) Muccioli, L.; D'Avino, G.; Berardi, R.; Orlandi, S.; Pizzirusso, A.; Roscioni, O. M.; Zannoni, C. *Top. Curr. Chem.* **2013**, DOI: 10.1007/128_2013_470.
(34) D'Avino, G.; Mothy, S.; Muccioli, L.; Zannoni, C.; Wang, L.; Cornil, J.; Beljonne, D.; Castet, F. *J. Phys. Chem. C* **2013**, *117*, 12981−12990.
(35) Yost, S. R.; Wang, L.; Van Voorhis, T. *J. Phys. Chem. C* **2011**, *115*, 14431−14436.
(36) Yost, S. R.; Van Voorhis, T. *J. Phys. Chem. C* **2013**, *117*, 5617−5625.
(37) Verlaak, S.; Beljonne, D.; Cheyns, D.; Rolin, C.; Linares, M.; Castet, F.; Cornil, J.; Heremans, P. *Adv. Funct. Mater.* **2009**, *19*, 3809−3814.
(38) Mothy, S.; Guillaume, M.; Idé, J.; Castet, F.; Ducasse, L.; Cornil, J.; Beljonne, D. *J. Chem. Phys. Lett.* **2012**, *3*, 2374−2378.
(39) Caruso, D.; Troisi, A. *Proc. Natl. Acad. Sci. U.S.A.* **2012**, *109*, 13498−13502.
(40) Soos, Z. G.; Tsiper, E. V. *Phys. Rev. B* **2001**, *64*, 195124.
(41) Cowan, S. R.; Banerji, N.; Leong, W. L.; Heeger, A. J. *Adv. Funct. Mater.* **2012**, *22*, 1116−1128.
(42) Orlandi, S.; Muccioli, L.; Ricci, M.; Berardi, R.; Zannoni, C. *Chem. Cent. J.* **2007**, *1*, 15.
(43) McMahon, D. P.; Cheung, D. L.; Troisi, A. *J. Phys. Chem. Lett.* **2011**, *2*, 2737−2741.
(44) Ochse, A.; Kettner, A.; Kopitzke, J.; Wendor, J. H.; Bassler, H. *Phys. Chem. Chem. Phys.* **1999**, *1*, 1757−1760.
(45) Holcombe, T. W.; Norton, J. E.; Rivnay, J.; Woo, C. H.; Goris, L.; Piliego, C.; Griffini, G.; Sellinger, A.; Brédas, J.-L.; Salleo, A.; Fréchet, J. M. *J. Am. Chem. Soc.* **2011**, *133*, 12106−12114.
(46) Fletcher, S. *J. Solid State Electrochem.* **2010**, *14*, 705−739.
(47) Jortner, J. *J. Chem. Phys.* **1976**, *64*, 4860−4867.
(48) Marcus, R. A. *Rev. Mod. Phys.* **1993**, *65*, 599−610.
(49) Engel, E.; Leo, K.; Hoffmann, M. *Chem. Phys.* **2006**, *325*, 170−177.
(50) Marciniak, H.; Li, X.-Q.; Würthner, F.; Lochbrunner, S. *J. Phys. Chem. A* **2011**, *115*, 648−654.
(51) Sukul, P.; Asthana, D.; Mukhopadhyay, P.; Summa, D.; Muccioli, L.; Zannoni, C.; Beljonne, D.; Rowan, A.; Malik, S. *Chem. Commun.* **2011**, *47*, 11858−11860.
(52) Liu, T.; Troisi, A. *Adv. Mater.* **2013**, *25*, 1038−1041.
(53) Olivier, Y.; Muccioli, L.; Lemaur, V.; Geerts, Y. H.; Zannoni, C.; Cornil, J. *J. Phys. Chem. B* **2009**, *113*, 14102−14111.
(54) Skabara, P. J.; Arlin, J.-B.; Geerts, Y. H. *Adv. Mater.* **2013**, *25*, 1948−1954.
(55) Yang, L. J.; Tan, C. H.; Hsieh, M. J.; Wang, J. M.; Duan, Y.; Cieplak, P.; Caldwell, J.; Kollman, P. A.; Luo, R. *J. Phys. Chem. B* **2006**, *110*, 13166.
(56) Marcon, V.; Vehoff, T.; Kirkpatrick, J.; Jeong, C.; Yoon, D. Y.; Kremer, K.; Andrienko, D. *J. Chem. Phys.* **2008**, *129*, No. 094505.
(57) Phillips, J. C.; Braun, R.; Wang, W.; Gumbart, J.; Tajkhorshid, E.; Villa, E.; Chipot, C.; Skeel, R. D.; Kale, L.; Schulten, K. *J. Comput. Chem.* **2005**, *26*, 1781−1802.
(58) Plimpton, S. *J. Comput. Phys.* **1995**, *117*, 1−19.
(59) Della Valle, R. G.; Andersen, H. C. *J. Chem. Phys.* **1992**, *97*, 2682−2689.
(60) Du, J.; Cormack, A. N. *J. Am. Ceram. Soc.* **2005**, *88*, 2532−2539.
(61) Cygan, R. T.; Liang, J.; Kalinichev, A. G. *J. Phys. Chem. B* **2004**, *108*, 1255−1266.
(62) Martinelli, N. G.; Idé, J.; Sanchez-Carrera, R. S.; Coropceanu, V.; Brédas, J.-L.; Ducasse, L.; Castet, F.; Cornil, J.; Beljonne, D. *J. Phys. Chem. C* **2010**, *114*, 20678−20685.
(63) McMahon, D. P.; Troisi, A. *J. Phys. Chem. Lett.* **2010**, *1*, 941−946.
(64) Castet, F.; Aurel, P.; Fritsch, A.; Ducasse, L.; Liotard, D.; Linares, M.; Cornil, J.; Beljonne, D. *Phys. Rev. B* **2008**, *77*, 115210.
(65) Coropceanu, V.; Cornil, J.; da Silva Filho, D. A.; Olivier, Y.; Silbey, R.; Brédas, J.-L. *Chem. Rev.* **2007**, *107*, 926−952.
(66) Silinsh, E. A.; Čápek, V. *Organic Molecular Crystals: Interaction, Localization, and Transport Phenomena*; AIP: New York, 1994.